PCCP

Accepted Manuscript




ROYAL SOCIETY OF CHEMISTRY

www.rsc.org/pccp

# TD-DFT Study of the Light-induced Spin Crossover of Fe(III) Complexes*

Sergi Saureu,[a] Coen de Graaf[a,b]

[a]Departament de Química Física i Inorgànica,
Universitat Rovira i Virgili, Marcel·lí Domingo s/n,
43007 Tarragona, Spain. E-mail: coen.degraaf@urv.cat

[b]Institució Catalana de Recerca i Estudis Avançats (ICREA)
Passeig Lluis Companys 23, 08010 Barcelona, Spain

November 27, 2015

*Electronic supplementary information (ESI) available: Coordinates and total energies of the optimized geometries of the $[Fe(qsal)_2]^+$ and $[Fe(pap)_2]^+$ complexes with different spin couplings. Graphical representation of the active orbitals and PBE0 frequencies and energy differences. See also: https://rodi.urv.es:8080/browse/handle/100000000/52

**Abstract**

Two light-induced spin-crossover Fe(III) compounds have been studied with time-dependent density functional theory (TD-DFT) to investigate the deactivation mechanism and the role of the ligand-field states as intermediates in this process. The B3LYP* functional has previously shown its ability to accurately describe (light-induced) spin-crossover in Fe(II) complexes. Here, we establish its performance for Fe(III) systems using $[Fe(qsal)_2]^+$ (Hqsal=2-[(8-quinolinylimino)methyl]phenol) and $[Fe(pap)_2]^+$ (Hpap=2-(2-pyridylmethyleneamino)phenol) as test cases comparing the B3LYP* results to experimental information and to multiconfigurational wave function results. In addition to rather accurate high spin (HS) and low spin (LS) state geometries, B3LYP* also predicts ligand-to-metal charge transfer (LMCT) states with large oscillator strength in the energy range where the UV-VIS spectrum shows an intense absorption band, whereas optically allowed $\pi$-$\pi^*$ excitations on the ligands were calculated at higher energy. Subsequently, we have generated a two-dimensional potential energy surface of the HS and LS states varying the Fe-N and Fe-O distances. LMCT and metal centered (MC) excited states were followed along the approximate minimal energy path that connects the minima of the HS and LS on this surface. The $^2$LMCT state has a minimum in the same region as the initial LS state, where we also observe a crossing with the intermediate spin (IS) state. Upon the expansion of the coordination sphere of the Fe(III) ion, the IS state crosses with the HS state and further expansion of the coordination sphere leads to the excited spin state trapping as observed in experiment. The calculation of the intersystem crossing rates reveals that the deactivation from $^2$LMCT$\rightarrow$IS$\rightarrow$HS competes with the $^2$LMCT$\rightarrow$IS$\rightarrow$LS pathway, in line with the low efficiency encountered in experiments.

# 1 Introduction

Over the last decades there has been considerable interest in spin crossover (SCO) and the associated molecular bistability of first-row transition metal (TM) complexes. The most widely studied complexes are based on the prototypical Fe(II)$N_6$ core, but other ions and coordination spheres are becoming more and more important in the field [1–3]. In fact, the first description of SCO concerned an Fe(III) complex [4], and nowadays many more Fe(III) complexes have been reported [5, 6]. The so-called light-induced excited spin state trapping (LIESST), which triggers the spin transformation from a low spin state (LS) to a metastable high spin state (HS) by light, has received special attention both in experimental and computational studies because it offers an optimal control on the SCO process. LIESST was discovered in the 1980s [7, 8] and explained shortly afterwards [9, 10]. Some necessary ingredients for LIESST are a not too large energy difference between the LS and HS states; significant different geometry of the two spin states and a correct ordering of the metal-to-ligand charge transfer (MLCT) and ligand-field states [11–13]. The less frequent occurrence of LIESST in Fe(III) complexes has always been ascribed to the relatively small modification of the iron coordination sphere when the electronic configuration changes from LS to HS. However, other factors such as $\pi$-$\pi$ intermolecular interactions between the ligands [14–19] have made possible the observation of SCO induced by light at reasonably high temperature and slow HS-LS relaxation in Fe(III) complexes.

Among the different Fe(II) complexes that show the LIESST phenomenon, $[Fe(bpy)_3]^{2+}$ (bpy = 2,2'-bipyridine) is one of the most intensely studied ones. Most experiments have been done at room temperature in aqueous solution [20–25]. After the initial laser pulse an excited singlet state with MLCT character is populated. This $^1$MLCT state was shown to deactivate on an extremely short time scale into the HS state. The system needs not more than $\sim$130 fs to reach a vibrationally hot quintet state. This HS state relaxes back to the initial LS state at a much longer time scale; the lifetime of the HS state is 650 ps. Although there is a clear consensus about the main characteristics of the photocycle, the role of the triplet ligand field (Fe-$3d^6$) states is still under debate. The first intersystem crossing from singlet to triplet takes place in the MLCT manifold

but it is not clear whether this state directly couples with the final HS state or that the deactivation goes via the triplet ligand field states. Arguments have been given for both scenarios [24–27] and it is obvious that more research is needed to clarify this issue.

The LIESST mechanism in Fe(III) complexes is much less profoundly analyzed. Experimental studies have not gone much further than the observation that the HS state gets populated after irradiation through magnetic susceptibility measurements [15–19, 28], but no time-resolved experiments have been published. From the theoretical point of view, we can mention the calculations by Ando and co-workers [29], who optimized the geometries of the different spin states of $[Fe(pap)_2]^+$ (Hpap = N-2-pyridylmethylidene-2-hydroxyphenylaminato), and calculated the vertical excitation energies and some aspects of the HS to LS deactivation. The present study makes a first step towards the detailed theoretical description of the LIESST process in Fe(III) complexes. From an accurate description of the fundamental LS state, we construct an approximate minimal energy path to the optimal geometry of the HS state and follow the energies of a large collection of excited states along this path to locate regions where intersystem crossing can take place and to explore the character of possible intermediate states in the LIESST process. Furthermore, we provide a rough estimate of the deactivation time by the calculation of the intersystem crossing rates with the time-dependent formulation of Fermi's golden rule [30]. The main focus is on $[Fe(qsal)_2]^+$ (Hqsal = N-(8-quinolyl)salicylaldimine), but we also pay attention to the $[Fe(pap)_2]^+$ complex. Both complexes are schematically depicted in Fig. 1.

## 2 Computational information

Despite the tremendous effort that has been made in the search of a density functional that is able to correctly reproduce the relative stability of high spin and low spin electronic configurations, there seems to be no consensus about the best strategy to accurately predict the adiabatic energy difference between HS and LS states in spin crossover complexes. Nevertheless, there are several functionals that have been tested for a large set of complexes and that turn out

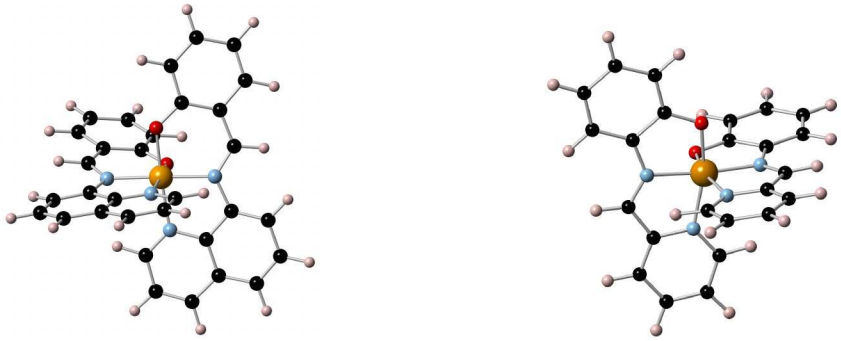

Figure 1: Ball and stick representation of the Fe(III) complexes: $[Fe(qsal)_2]^+$ (left), $[Fe(pap)_2]^+$ (right). Color code: orange for Fe, red for O, black for C, blue for N and pink for H.

to work rather satisfactorily, examples are OPBE, TPSSh and B3LYP* [31–33]. The latter functional reduces to 15% the exact Fock exchange in the standard B3LYP functional. This reduction is based on the observation that $\Delta E_{HL}$ depends linearly on the amount of Fock exchange in the functional. Whereas the original B3LYP systematically overestimates the stability of the HS state, reducing the Fock exchange to 15% brings the calculated relative stability in agreement with experiment for a large collection of SCO complexes. For an accurate computational description of light-induced SCO it is also important to have good geometries and accurate estimates of the vertical excitation energies. These two aspects have been tested by Papai and co-workers for three Fe(II) complexes [34] and it was concluded that the B3LYP* functional leads to geometries as accurate as obtained with virtually any other choice, but more importantly also reproduces rather well the potential energy curves of ground and excited states using the time-dependent variant of DFT. This made us decide to use this functional to explore the LIESST mechanism in the two Fe(III) complexes mentioned before. To establish the performance of the functional with respect to the calculated geometries and vibrational frequencies, we compare the results to those obtained with the PBE0 functional (more details in Section 3 of the Supporting Information), which was previously used in the study of the deactivation mechanism in $[Fe(bpy)_3]^{2+}$ [35]. The adiabatic energy differences and vertical excitation energies are compared to experimental data

when available and to results of multiconfiguration wave function calculations, specifically complete active space self-consistent field (CASSCF) followed by CAS second-order perturbation theory (CASPT2).

All B3LYP* calculations have been performed with the ORCA program package version 3 [36]. Both for the geometry optimizations and the TD-DFT calculations, the def2-TZVP [37] basis set (triple zeta for the valence plus polarization functions on all atoms) was used. To reduce the computational cost implicit to the use of hybrid functionals, we have activated the RIJCOSX procedure [38] to speed-up the calculation of the exchange contribution to the energy. Vibrational frequencies were calculated by numerical differentiation of the analytical gradients for the lowest states of each spin symmetry (doublet, quartet and sextet) and fully numerically for the first lowest excited doublet state of ligand-to-metal charge transfer character [39]. In the latter case, we have reduced the basis set to split-valence quality (def2-SV(P) [37]) and increased the convergence criteria to avoid spurious imaginary frequencies. The effect of the basis set reduction on the vibrational frequencies was tested by repeating some of the calculations for the fundamental states with this smaller basis. The calculations with the PBE0 functional (the hybrid variant of the PBE functional with 25% Fock exchange) [40] were performed with TurboMole 6.6 [41–44] using the same def2-TZVP basis set as before.

In addition to the full geometry optimization we also generated a two-dimensional potential energy surface by performing a series of restricted geometry optimizations in which the Fe-O and Fe-N distances were kept fixed while the rest of the complex was fully relaxed. The Fe-O distance was fixed at different values in the interval of 1.80 to 2.00 Å and the Fe-N distance was varied in the 1.85–2.30 Å interval. This surface contains the HS and LS minimal structures and allows us to define an approximate minimal energy path to interpolate between the two minima. The evolution of the excited state energies was followed along this interpolation path to find the approximate location of intersystem crossings from the excited doublet state to quartet and sextet states and in this way obtain information about the character of the intermediates in the LIESST process.

CASSCF/CASPT2 calculations were performed as implemented in the MOL-

CAS 7.4 package [45]. Atomic natural orbital (ANO) basis sets optimized for scalar relativistic effects and core correlation were applied for all atoms [46, 47]. For both complexes we used a (7s,6p,5d,4f,3g,2h) contraction for Fe, (4s,3p,1d) for N and O, (3s,2p) for C and (2s) for H. The Cholesky decomposition [48, 49] was used to reduce the computational cost associated to the calculation of the two-electron integrals. Scalar relativistic effects were included using Douglas-Kross-Hess Hamiltonian [50]. Spin-orbit coupling (SOC) and oscillator strengths of the electronic transitions were calculated with the state interaction approach [51–53].

Two active spaces were used to construct the CASSCF reference wave function depending on the transitions studied. The first active space contains 9 electrons distributed in all possible ways over 12 orbitals; five orbitals with mainly Fe-3d character, two $\sigma$-bonding orbitals with important contributions on the lone pairs of N and O, and five orbitals that account for the double shell effect of the 3d-shell, the so-called 3d' orbitals. This active space has been used in many applications on TM complexes before and provides a balanced description of all the important non-dynamic electron correlation [53–55]. It has been used to build the two-dimensional CASPT2 potential energy surface of the LS and HS states. The second active space extends the previous one with two ligand $\pi$ orbitals leading to an active space of 14 orbitals and 13 electrons. The inclusion of these orbitals permits us to study the electronic excited state with LMCT character, which turned out to be the lowest optically allowed transitions in contrast to the $[Fe(bpy)_3]^{2+}$ complex where the lowest excited states have metal-to-ligand charge transfer character. More information about the shape of the active orbitals can be found in the Supporting Information, Figure S1.1 and S4.1.

CASPT2 calculations account for the remaining electron correlation by correlating all the electrons except the deep core electrons ($1s^2$ for N, O and C and $1s^2 2s^2 2p^6$ for Fe). In order to exclude possible intruder states, we applied an imaginary level shift of 0.15 a.u. in CASPT2 [56]. The standard definition of the zeroth-order Hamiltonian (IPEA=0.25) was used. Moreover, three more IPEA values, 0.00, 0.50 and 0.70, have been tested to check the influence of this parameter on the adiabatic CASPT2 energies [57].

# 3 Results and Discussion

## 3.1 Geometry, vibrational frequencies and energetics

The geometries were fully optimized for the lowest spin-states of the $3d^5$ configuration of the $Fe^{3+}$: the doublet and the sextet. The DFT calculations for the doublet and sextet were performed within the spin-unrestricted formalism, and hence, the resulting electronic states are not necessarily eigenfunctions of the $\hat{S}^2$ operator. However the spin functions considered here are essentially mono-determinantal and the spin contamination is very small. The expectation values of $\hat{S}^2$ for HS and LS, 8.76 and 0.77, are close to the formal values of 8.75 and 0.75.

Table 1 shows the optimized bond lengths of the central Fe(III) ion to the six atoms in the first coordination sphere of the two complexes. The structures are slightly distorted from the ideal octahedral coordination with shorter Fe-O bonds than the Fe-N ones, which in turn appear in pairs. The distances are in good agreement with experiment, albeit slightly overestimated. The largest deviation is observed for the Fe-N bond length in the HS state of $[Fe(qsal)_2]^+$, which is 0.09 Å longer than the experimental value. All other distances differ by less than 0.05 Å. The expansion of the coordination sphere is nicely reproduced by the DFT calculations; the Fe-O distance is hardly affected by the change in the spin state, while the Fe-N distances change by approximately 0.2 Å. The DFT calculations also reproduce the angles in the Fe coordination sphere rather accurately, Table S2.1 and S5.1 of the supporting information shows that none of the calculated angles differs by more than 5° from the experimental value, both in the LS and the HS geometry.

The expansion of the Fe coordination sphere in the prototypical $Fe(II)N_6$ spin-crossover materials is known to strongly affect the frequencies of the vibrational modes dominated by the stretching of the Fe–N bonds. In general, these modes get softer by about 50-120 $cm^{-1}$ in the HS state, which gives a major contribution to the increased entropy of the HS state [58]. A similar change in the vibrational modes is also observed in the DFT calculations on the two Fe(III) complexes studied here. Table 2 shows a selection of HS and LS vibrational frequencies, which imply important displacements in the $FeN_4O_2$ core of

Table 1: B3LYP*/def2-TZVP optimized bond lengths in Å of $[Fe(qsal)_2]^+$ and $[Fe(pap)_2]^+$. The experimental distances in parenthesis are taken from Ref. [16].

| $[Fe(qsal)_2]^+$ | | | |
|---|---|---|---|
| distance | HS | LS | Δr |
| Fe–O | 1.91 (1.88) | 1.88 (1.88) | 0.03 (0.00) |
| Fe–$N_1$ | 2.21 (2.12) | 2.02 (1.97) | 0.19 (0.15) |
| Fe–$N_2$ | 2.18 (2.09) | 1.97 (1.94) | 0.21 (0.25) |
| $[Fe(pap)_2]^+$ | | | |
| distance | HS | LS | Δr |
| Fe–O | 1.93 (1.93) | 1.88 (1.88) | 0.05 (0.05) |
| Fe–$N_1$ | 2.25 (2.21) | 2.01 (1.99) | 0.24 (0.22) |
| Fe–$N_2$ | 2.18 (2.17) | 1.93 (1.91) | 0.25 (0.26) |

the complex. The vibrations are marked as bending or stretching and in the latter case we also put a symmetry label on the vibrations. This is, however, to some extent arbitrary since the complex only has an approximate octahedral symmetry and the vibrations turn out to be mixtures of bending and stretching modes, with contributions not only of the $FeN_4O_2$ core, but also coupled to movement on the ligands. For this reason it has not been possible to assign the symmetric breathing mode in the HS state of $[Fe(pap)_2]^+$.

The stretching modes labeled $t_{1u}$ are characterized by an off-center movement of the Fe ion and it is exactly in these modes that the largest difference between the LS and HS state is observed. The $t_{1u}$ frequencies are lowered by 115 and 95 $cm^{-1}$ on average in $[Fe(qsal)_2]^+$ and $[Fe(pap)_2]^+$, respectively. The frequencies of the other vibrations are also lower but the change is in general significantly smaller.

To close this exploration of the ground state properties, we report the adiabatic energy difference of the LS and HS state $\Delta E_{HL}$. This key parameter is notoriously difficult to calculate with DFT methods given the strong dependency of the results on the functional applied, but even for multiconfigurational

Table 2: Frequencies in $cm^{-1}$ of the Fe-L bending and stretching modes for the LS and HS states of $[Fe(qsal)_2]^+$ and $[Fe(pap)_2]^+$. The labels of the stretching modes are approximate due to the non-ideal octahedral symmetry.

| | $[Fe(qsal)_2]^+$ | | $[Fe(pap)_2]^+$ | |
|---|---|---|---|---|
| Character | LS | HS | LS | HS |
| Bending | | | | |
| | 164 | 133 | 168 | 95 |
| | 184 | 141 | 179 | 152 |
| | 200 | 185 | 209 | 175 |
| | 224 | 193 | 261 | 235 |
| | 233 | 210 | 280 | 246 |
| Stretching | | | | |
| $e_g$ | 218 | 222 | 241 | 227 |
| $e_g$ | 256 | 239 | 250 | 231 |
| $a_g$ | 259 | 226 | 252 | – [a] |
| $t_{1u}$ | 342 | 260 | 333 | 271 |
| $t_{1u}$ | 353 | 261 | 336 | 272 |
| $t_{1u}$ | 385 | 308 | 441 | 281 |

(a) The symmetric stretch (or breathing mode) could not be identified.

wave function based calculations there is some debate on the most reliable (efficient) procedure to calculate this property. As stated in the Introduction, the B3LYP* functional was specifically designed to reproduce $\Delta E_{HL}$ in Fe(II) complexes. Our present results show that the functional also performs rather well for the here considered Fe(III) complexes. In both cases the LS electronic energy is lower than the HS energy, in agreement with the LS character of both complexes at room temperature and below (contrary to the PBE0 results, see Table S3.3). A direct validation of the size of the calculated $\Delta E_{HL}$ is difficult, since this parameter is not easily extracted from experiment. Hence, we opt for an indirect comparison with experiment via the transition temperature of the thermal spin crossover $T_{1/2}$ [14, 16, 59]. Following the procedure outlined in

previous studies [58, 60–64], we calculated $T_{1/2}$ by adding the zero-point energy to the electronic energy of both states and look for the temperature at which the $T\Delta S$ product is equal to the enthalpy. The entropy change is dominated by the vibrational contribution but has a small constant contribution due to the different spin multiplicity of the LS and HS states of 9.13 J $K^{-1}$ $mol^{-1}$ (0.76 $cm^{-1}/K$). Table 3 lists the DFT adiabatic HS–LS energy differences, the zero-point energy contribution and the sum of these two terms ($\Delta H_{HL}$) for the two complexes. The resulting $T_{1/2}$ are in qualitative agreement with the experimental values of the transition temperatures, which adds additional evidence for the reliability of the B3LYP* functional for determining the relative energies of the electronic states involved in the spin crossover process in Fe(III) complexes. The overestimation of the transition temperature is most probably a combination of uncertainty in the calculated $\Delta E_{HL}$ and the lack of environment effects, which play an important role due to the $\pi$-$\pi$ interactions between the ligands on neighboring complexes. Note that these interactions also cause the hysteresis and the two-step nature of the thermal spin crossover. The theoretical description of these phenomena goes beyond the scope of the present paper. Here, the focus is on the light-induced variant, and more specifically on the initial stages of the process to obtain information about the deactivation mechanism from excited LS state to metastable HS state. This process is much less dependent on the environment and can be studied in isolated complexes.

Table 3: Adiabatic HS-LS energy difference ($\Delta E_{HL}$), difference in zero-point energy ($\Delta ZPE$) and theoretical estimate of the transition temperature for thermal spin crossover of $[Fe(qsal)_2]^+$ and $[Fe(pap)_2]^+$. Energies in $cm^{-1}$, temperature in K. Experimental data in parenthesis [14, 16, 59].

| | $[Fe(qsal)_2]^+$ | $[Fe(pap)_2]^+$ |
|---|---|---|
| $\Delta E_{HL}$ (DFT) | 2166 | 2127 |
| $\Delta ZPE$ | -670 | -660 |
| $\Delta H_{HL}$ | 1496 | 1467 |
| $T_{1/2}$ | 350 (289-205) | 324 (181-165) |

### 3.2 Potential energy surfaces for LS and HS

The largest changes in the geometry between the doublet and sextet states take place in the first coordination sphere of the Fe(III) ion and lead to an increase of the radius of the coordination sphere by approximately 0.15 Å. This expansion largely determines the potential energy surface on which the SCO takes place, but other more subtle geometric changes also play a role in facilitating the thermal SCO or the deactivation of the excited LS state in LIESST [65, 66]. By performing a series of restricted geometry optimizations, a two-dimensional potential energy surface has been constructed as explained in the computational information. Figure 2 shows the B3LYP* energies on this grid for the spin state with the lowest energy, *i.e.* the doublet state for the smaller distances and the sextet state for the part of the surface with larger Fe-O and Fe-N distances. The surface was constructed with 400 points and the contours in the figure are interpolations, which should be considered as a guide to the eye. For both complexes, the line that connects the two minima can be considered within a rather good approximation as the minimal energy path and we will use it as reaction coordinate to follow the deactivation of the excited LS state towards the meta-stable HS state.

This reaction coordinate not only involves the expansion of the coordination sphere but also includes all other geometric changes between the LS and HS state, among which the opening of the O-Fe-N angle is one of the most important ones (see Table S2.1). Therefore, the representation of the potential energy surface in terms of the Fe-N and Fe-O distances is just one of the many possible. Alternatively one could also choose the Fe-N distance and the O-Fe-N angle as coordinates to explore the ground state energy surface as is done in Fig. 3 for $[Fe(qsal)_2]^+$ (the representation for the other complex can be found in the supporting information, Fig. S7.1). The approximate minimal energy path from LS to HS in this representation is also nearly linear although a certain decoupling of the enlargement of the Fe-N distance and the opening of the O-Fe-N distance can be observed on the potential energy surface. This two-mode model has also been invoked in the spin crossover mechanism in Fe(II) complexes both for the thermal [10, 34] and the light-induced variant [67, 68]. The two-mode deactivation mechanism requires an extensive exploration of the excited state

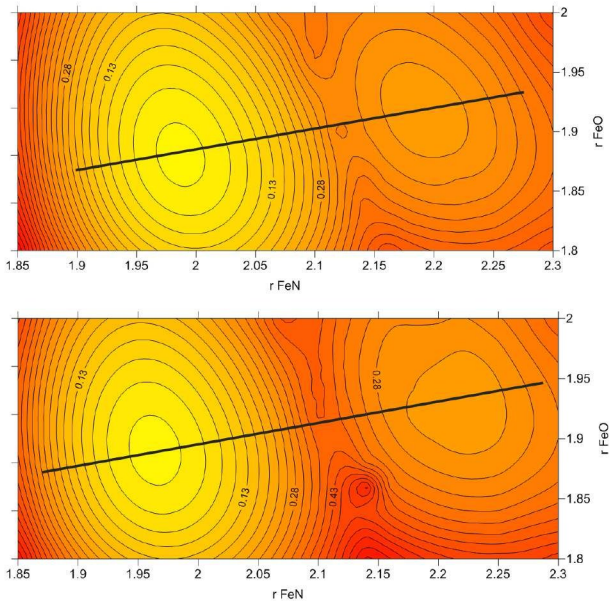


Figure 2: B3LYP* potential energy surface as function of the Fe-N and Fe-O distances (Å) of the lowest electronic state of $[Fe(qsal)_2]^+$(top) and $[Fe(pap)_2]^+$(bottom). The black thick line indicates the quasi minimal energy path (MEP) connecting the LS minimum on the left to the HS minimum on the right. Energies (in eV) are relative to the total energy of the LS minimum.

potential energy surfaces, which will be subject of a follow-up study.

CASPT2 calculations can give accurate excitation energies provided that the active space and basis set are properly chosen. Additionally, it has been shown in previous works on Fe(II) complexes that it is essential to re-optimize the distances between Fe and its first neighbours [35, 55, 69]. The use of DFT optimized geometries can easily lead to errors larger than 1 eV. This is caused by the fact that CASPT2 has the tendency to shorten the Fe-L distances, which leads to stronger ligand field and consequently higher MC excited states. The effect on the LMCT (and MLCT) states is less drastic since the electronic configuration of these states does normally not contain electrons in the anti-bonding Fe-3d($e_g$) orbitals as it is also the case for the LS ground state. A full geometry optimization of the whole complex with CASPT2 is beyond the current computational possibilities and therefore we opt for single point CASPT2 calculations

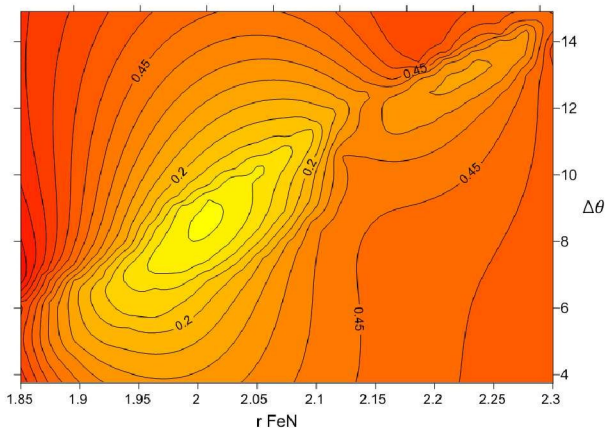


Figure 3: B3LYP* potential energy surface of the lowest electronic state of $[Fe(qsal)_2]^+$ as function of the Fe-N distance (Å) and $\Delta\phi$ (degrees), the difference in the O-Fe-N angle between LS and HS.

on a selection of points generated with the restricted DFT geometry optimizations to find the optimal Fe-N and Fe-O distances for $[Fe(qsal)_2]^+$. There is ample evidence that the CAS(9,12) and the basis set specified in the computational information are sufficiently large to give close to converged estimates of the optimal CASPT2 distances [55, 57, 64, 70, 71].

The CASPT2 potential energy surface shown in Fig. 4 is less well defined than the ones that were constructed from the DFT data due to the smaller number of points, but the graph shows that the energy surface has the same shape as the DFT/B3LYP* one, with the difference that the minima for both LS and HS state appear at smaller Fe-ligand distances. The minimum of the LS state is located at 1.93 Å and 1.82 Å for the Fe-N and Fe-O distances, respectively. These distances increase by 0.19 Å for the Fe-N and 0.04 Å for the Fe-O distance in the HS minima, being the $\Delta r_{HL}$ very similar to the experimental increase. For the complex $[Fe(pap)_2]^+$, we located the minimum of the LS state at 1.89 Å and 1.84 Å for the Fe-N and Fe-O distances, respectively. The variation of the Fe-N distance in the HS minima is 0.04 Å larger than the complex $[Fe(qsal)_2]^+$ and it is equal for the Fe-O distance, locating this minima at 2.12 Å and 1.88 Å respectively.

The CASPT2 adiabatic HS-LS energy difference at the geometry with the

Table 4: CASPT2 $\Delta E_{HL}$ values (in $cm^{-1}$) calculated with different IPEA values in the definition of $\hat{H}^{(0)}$ using the B3LYP* optimized geometry or the geometry with CASPT2 reoptimized Fe–ligand distances.

| Geometry | IPEA | $\Delta E_{HL}$ | |
|---|---|---|---|
| | | $[Fe(qsal)_2]^+$ | $[Fe(pap)_2]^+$ |
| B3LYP* | 0.00 | -628 | -53 |
| | 0.25 | 2050 | 2742 |
| | 0.50 | 3877 | 4548 |
| | 0.70 | 5133 | 5780 |
| + reopt. d(Fe–L) [a] | 0.25 | 1658 | 2157 |

(a) Fe–ligand distances are reoptimized with CASPT2

relaxed Fe-O and Fe-N distances is 1658 and 2157 $cm^{-1}$, respectively, as shown in the last entry of Table 4. This is in a good agreement with the B3LYP* adiabatic energy difference listed in Table 3. To complete the comparison between CASPT2 and DFT, we looked at the proposal of Kepenekian *et al.* [57] to calculate $\Delta E_{HL}$. They observed that the CASPT2 $\Delta E_{HL}$ values calculated with the standard zeroth-order Hamiltonian $\hat{H}^{(0)}$ are systematically underestimated for Fe(II) complexes and found that increasing the IPEA values greatly improves the theoretical estimate of this quantity. This was later confirmed by Lawson Daku and co-workers [72]. However, in the present case the recipe of increasing the IPEA value does not give the desired result. The effect is similar to what is observed in the Fe(II) complexes –increasing the IPEA favors the LS state with respect to the HS state– but the calculated $\Delta E_{HL}$ becomes so large that thermal spin crossover near room temperature is no longer viable. For example, using the values obtained with IPEA=0.50, the theoretical estimate of $T_{1/2}$ becomes larger than 700 K, which is clearly outside the experimental range. On the other hand, it can be seen from the Table 4 that the definition of the zeroth-order Hamiltonian in the original CASPT2 papers from the early 1990s [54, 73] fails to predict the LS as ground state.

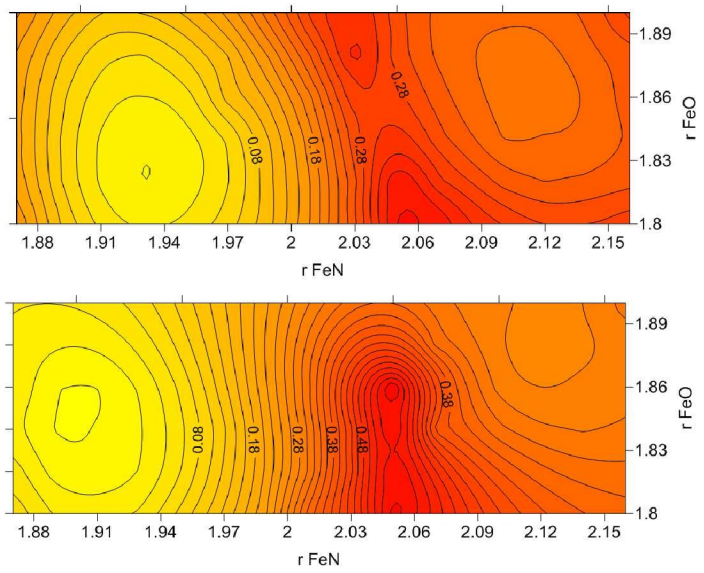


Figure 4: CASPT2 potential energy surface as function of the Fe-N and Fe-O distances (Å) of the lowest electronic state in the complexes $[Fe(qsal)_2]^+$ (top) and $[Fe(pap)_2]^+$ (bottom). Energies (in eV) are relative to the total energy of the LS minimum.

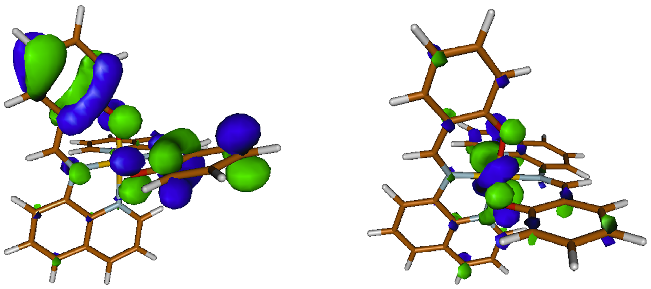

Figure 5: Graphical representation of the orbitals involved in LMCT transition of $[Fe(qsal)_2]^+$; *left*: the ligand $\pi$ orbital that looses one electron, *right*: the Fe-3*d* orbital of $t_{2g}$-like character that receives the electron.

### 3.3 Absorption spectrum

To study the deactivation mechanism from the initially populated excited LS state to the metastable HS state we cannot stay on the ground state energy surfaces, and therefore, we will now switch attention to the excited states. The most two common low-lying excitations for Fe(III) complexes are: (i) the metal centered (MC) transitions involving electron replacements within the Fe-3d orbitals and (ii) the ligand-to-metal charge transfer (LMCT) transitions transferring one electron from the $\pi$ system of the ligand to the iron center, as illustrated in Fig. 5. The higher formal oxidation state of Fe makes that the metal-to-ligand charge transfer, dominant at low energies in the more commonly studied Fe(II) complexes, lies at higher energies and therefore less important for the spin crossover. The $\pi$-$\pi^*$ excitations on the ligands also lie at higher energy than the LMCT transitions.

Figure 6 displays the B3LYP* absorption spectrum of $[Fe(qsal)_2]^+$ (*top*) and $[Fe(pap)_2]^+$ (*bottom*) in their LS ground state. The curves are obtained by representing each transition by a gaussian function with a full-width at half-maximum of 40 nm and a height that corresponds to the relative oscillator strength. Starting with $[Fe(qsal)_2]^+$, the main peak at 724 nm is dominated by LMCT transitions and is in good agreement with the experimental wave length of 803 nm used to induce the spin crossover. At lower energy one can

find the MC transitions, but these have much lower oscillator strengths and do not contribute to the absorption spectrum. At higher energy, between 615-470 nm, we observe other intense bands, which can be ascribed to ligand-ligand excitations. Unfortunately, we are not aware of any experimental absorption spectrum in the literature of this complex and therefore a direct comparison with experiment is not possible. However, a similar broad band around 724 nm has been reported in the literature for other Fe(III) complexes with spin crossover, for example $Fe(acpa)_2$ and $Fe(Sal_2tr)$ [74, 75]. In these two complexes the LMCT is found at slightly higher energy, 685 and 620 nm respectively. The absorption spectrum of $[Fe(pap)_2]^+$ has the same overall shape. The most significant difference is the shift to lower energies of the main LMCT band to 820 nm and the increased LMCT character of the band between 500-550 nm. This is in agreement with experiment, since LIESST is triggered with 532 nm light in this compound.

We also compared the vertical excitation energies obtained with B3LYP* to those calculated with CASPT2. For this purpose the active space was extended with two occupied ligand $\pi$-orbitals resulting in a CAS(13,14). Using the geometry with the re-optimized Fe–ligand distances, the lowest LMCT state appears at 578 nm in complex $[Fe(qsal)_2]^+$ and at 354 nm for $[Fe(pap)_2]^+$. Both transition energies are significantly higher than those found in the TD-DFT calculations and used in the LIESST experiments. A possible explanation lies in the symmetry of the complexes. The two-fold rotation axes forces the ligand-$\pi$ orbital involved in the LMCT process to be delocalized over both ligands. As found by Domingo *et al.* [76], the inclusion of the effect of the thermal motion leads to a constant symmetry breaking and consequently two inequivalent ligands. The localization of the orbital involved in the CT excitation on one of the ligands was shown to lower the excitation energy significantly. To avoid lengthy molecular dynamics simulations and subsequent CASPT2 calculations on a series of snapshots as done in Ref. [76], we distort the geometry of the complex by hand shortening the Fe-ligand distance by 0.2 Å for one of the ligands. Figure 7 shows how this distortion leads to a localization of the ligand $\pi$ orbital and induces a lowering of the excitation energy in complex $[Fe(qsal)_2]^+$ to 775 nm, in much better agreement with the experimental value. Doing the same trick in

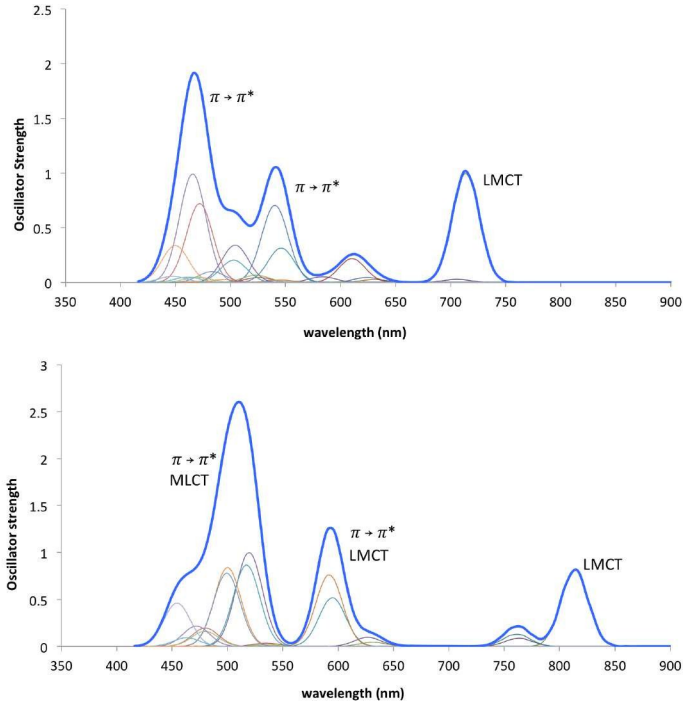


Figure 6: B3LYP* absorption spectrum of $[Fe(qsal)_2]^+$ (top) and $[Fe(pap)_2]^+$ (bottom). The individual transitions (thin lines) are represented by a Gaussian function ($bw = 40$ nm). Oscillator strength in arbitrary units.

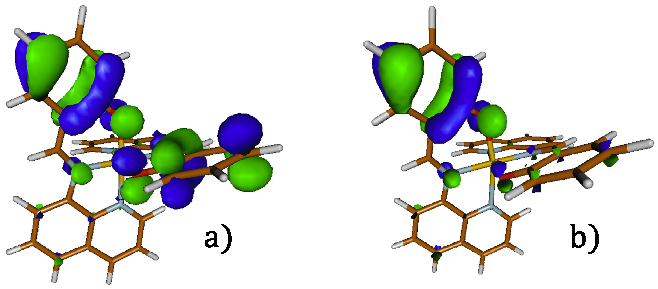


Figure 7: Graphical representation of the ligand $\pi$ orbital involved in the LMCT transition of the $[Fe(qsal)_2]^+$ complex. a) Delocalized orbital over two ligands with non-distorted geometry. b) Localized orbital over one ligand with distorted geometry.

the TD-DFT calculation lowers the LMCT energy to 820 nm, still in excellent agreement with CASPT2 and experiment.

### 3.4 Excited states along the quasi minimal energy path

In analogy to the study of the LIESST phenomenon in Fe(II) complexes [27, 35, 70, 71], we constructed the potential energy curves of the ground and excited states along the approximate minimal energy path that connects the LS and HS minima shown in Fig. 2 as a thick black line. At regular intervals on this line, TD-DFT calculations were performed to follow the evolution of the relative energies of a collection of excited states. The results are shown in Fig. 8. The two figures share the same main characteristics. At short Fe–L distances both complexes have a doublet ground state dominated by the Fe-$3d^5$ configuration shown in the upper left panel of Fig. 9. The other two components of this electronic configuration –degenerate with the ground state in a perfect octahedral surrounding– lie approximately 0.6 eV higher in energy. This relative energy between the different components of the LS state ($^2T_{2g}$ in $O_h$ symmetry) was also obtained with CASPT2. At larger distances, the ground state corresponds to the HS state ($^6A_{1g}$ in $O_h$ symmetry) with an electronic configuration shown in the upper right panel of Fig. 9. This state rapidly increases in energy with

decreasing distance and lies way up in energy in the Franck-Condon region of the doublet ground state. At lower energy, we can observe a quartet state with a Fe-3$d^5$ configuration (upper-middle panel in Fig. 9). The fact that this state has only one electron in the antibonding $e_g$-like orbitals causes this state to have a minimum somewhere between the distances where the doublet and sextet have their lowest energy. Note that this intermediate spin (IS) state lies rather close in energy to the crossing point of the LS and HS state as earlier observed by Ando [29] in $[Fe(pap)_2]^+$ and by Iuchi [77] in the Fe(II) complex $[Fe(bpy)_3]^{2+}$. The other components of the lowest IS ($^4T_{1g}$ in $O_h$ symmetry) lie slightly higher and can be recognized in the Fig. 8 as the two grey lines parallel to the thick green line at approximately 0.3 and 0.5 eV higher energy.

The other low-lying states are doublets of LMCT character, whose electronic configuration can be found in the left lower panel of Fig. 9. These states have the strongest oscillator strength and are populated when the system is irradiated with light. The potential energy curves of these states are parallel to the metal centered doublets since both have zero electrons in the Fe-3$d$ $e_g$-like orbitals. The quartet LMCT states lie at significant higher energy and are not expected to play any role in the deactivation process from $^2$LMCT to HS. This is quite different from the mechanism generally accepted for the Fe(II) complexes, where the first intersystem crossing takes place in the MLCT manifold. The quartet LMCT states lie higher in energy than the doublets LMCTs because unavoidably one of the Fe-3$d$ $e_g$-like orbitals has to be occupied to form a quartet state (Fig. 9, *right*), which is not the case for the doublet LMCTs.

### 3.5 Deactivation rates in Fe(III) complexes

The shape of the potential energy curves suggests that the deactivation of the $^2$LMCT state involves an intersystem crossing with the metal centered quartet state followed by an intersystem crossing with the final metastable HS state. To give support for this deactivation path we estimate the intersystem crossing rates using the time dependent formulation of Fermi's golden rule [30] and successfully applied to describe the photocycle in $[Fe(bpy)_3]^{2+}$ [27]. Vibrational frequencies and normal modes were determined for the LS, IS, and HS states in an ordinary DFT treatment, while the $^2$LMCT state was addressed with

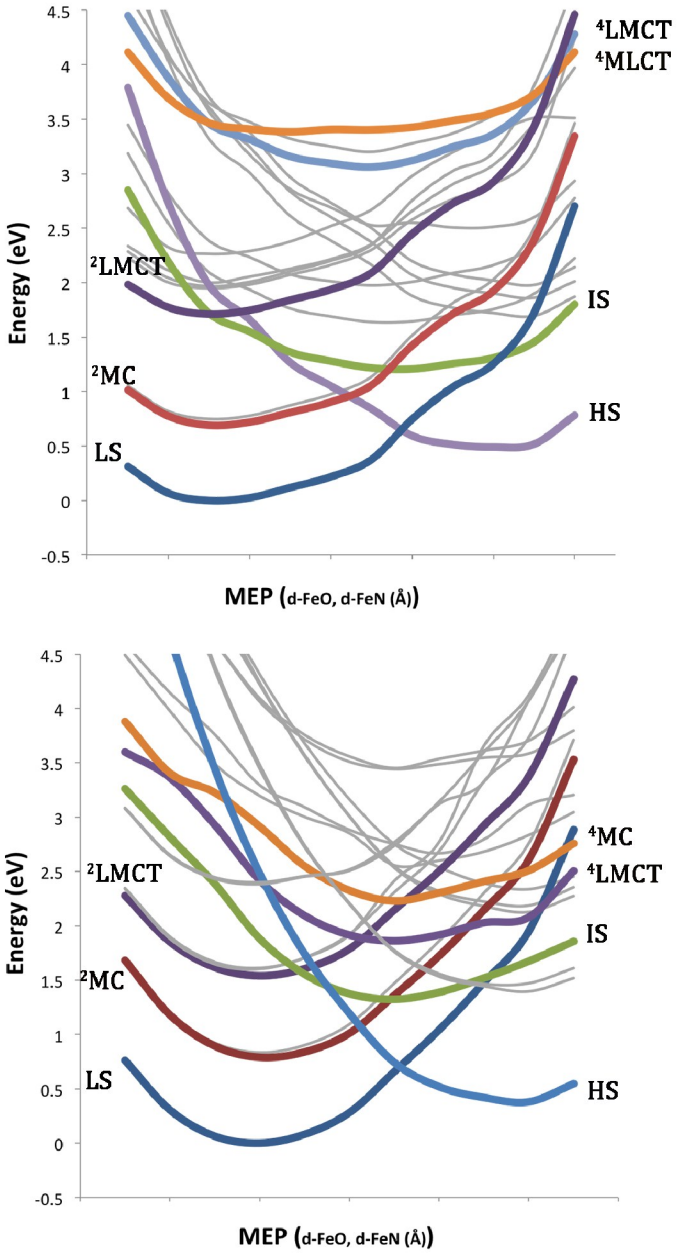


Figure 8: B3LYP* potential energy curves for a collection of electronic states along the quasi-MEP of the complexes $[Fe(qsal)_2]^+$ and $[Fe(pap)_2]^+$.

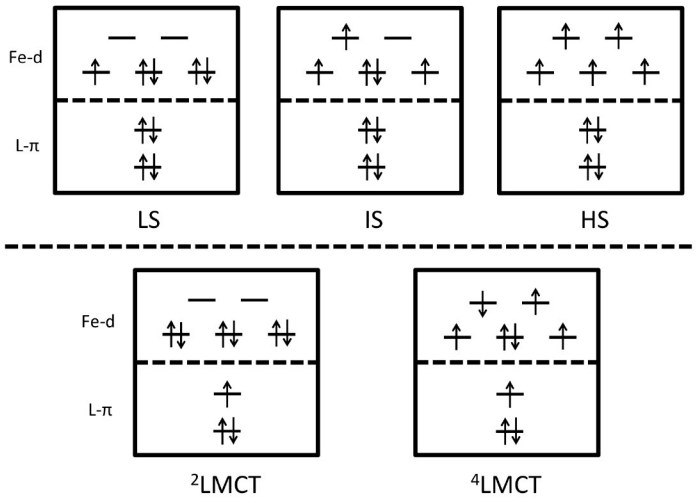


Figure 9: Schematic representation of the electronic configurations of the states involved in the LIESST phenomenon.

TD-DFT. Combined with the energy differences and the spin-orbit coupling among these four states, the crossing rates were determined, and from these the lifetimes of the excited states. As stated in the computational information, the spin-orbit coupling among the different states was calculated through the state interaction using the CASSCF wave functions. The use of an effective one-electron spin-orbit operator [78] makes the direct coupling between states that differ by more than one electron in the leading electronic configuration very small (or even zero). Therefore, we also consider second-order effects, that is the coupling between $\Psi_I$ and $\Psi_J$ involving other intermediate states. Instead of using the perturbative expression applied by Iuchi in the study of the spin-orbit coupling in $[Fe(bpy)_3]^{2+}$ [77], we have included this indirect coupling in a variational manner with the effective Hamiltonian approach. The full spin-orbit matrix with 14 doublets, 15 quartets and 8 sextet states is mapped on a smaller model space that only contains the LS, IS, HS and $^2$LMCT states. The matrix elements of the effective Hamiltonian shown in Table 5 include not only the direct spin-orbit coupling between the states of the model space, but also the effect of the indirect coupling via the external states [79].

Table 5: Effective spin-orbit coupling matrix elements $\langle\Phi_I|\hat{H}_{SO}^{eff}|\Phi_F\rangle$ of the complex $[Fe(qsal)_2]^+$ at the B3LYP* optimized geometry of the LS state.

| $\Phi_I$ | $\Phi_F$ | SO coupling ($cm^{-1}$) |
|---|---|---|
| $^2$LMCT | IS | 15.0 |
| $^2$LMCT | HS | 3.4 |
| IS | HS | 368.1 |
| IS | LS | 347.0 |
| HS | LS | 8.9 |

Starting with the $^2$LMCT state, there are several possible deactivation paths. The small spin-orbit coupling with the HS state makes the direct deactivation of the excited state highly improbable. Alternatively the $^2$LMCT may undergo an internal conversion and fall back in the initial LS state. This will certainly happen, but we cannot calculate the rate of this process, since Fermi's golden rule only gives us access to intersystem crossing rates. To address the internal conversions one has to rely on more sophisticated simulation techniques like multiconfigurational time-dependent Hartree (MCTDH) simulations or ab initio molecular dynamics with surface hopping [80–86]. Remains the intersystem crossing with the IS state. The rather small spin-orbit coupling is solely due to second-order coupling, since the leading electronic configurations of the two states differ by more than one electron (see Fig. 9) making the direct coupling practically zero. However, this small coupling is partially compensated by a rather large vibrational contribution and we obtain a reasonably high intersystem crossing rate.

After reaching the IS state, the system can further evolve either by an intersystem crossing with the HS state to complete the LIESST path, or fall back on the initial LS state. The calculated intersystem crossing rates show that both processes are extremely fast and compete. This means that the quantum yield of the LIESST process can never be as high as found in the polypyridyl Fe(II) complexes, where the quantum yield is reported to be unity. This is, however, not the case in the here-considered Fe(III) complexes. Experimental

studies point at a much lower efficiency. Once the system reaches the HS state, it becomes trapped; the intersystem crossing rate with the LS state is small.

Table 6: Intersystem-crossing rates between all states of the $[Fe(qsal)_2]^+$ involved on the LIESST phenomenom.

| $\Phi_I$ | $\Phi_F$ | SO term [$cm^{-2}$] | Vibrational term [$cm^2s^{-1}$] | t [s] |
|---|---|---|---|---|
| $^2$LMCT | IS | $2.26 \times 10^2$ | $7.94 \times 10^8$ | $1.26 \times 10^{-9}$ |
| $^2$LMCT | HS | $1.14 \times 10^1$ | $5.54 \times 10^7$ | $1.81 \times 10^{-8}$ |
| IS | HS | $1.35 \times 10^5$ | $2.45 \times 10^{13}$ | $4.08 \times 10^{-14}$ |
| IS | LS | $1.20 \times 10^5$ | $6.66 \times 10^{12}$ | $1.50 \times 10^{-13}$ |
| HS | LS | $7.89 \times 10^1$ | $5.01 \times 10^5$ | $1.99 \times 10^{-6}$ |

A graphical representation of the deactivation pathway that arises from our calculations is given in Fig. 10. It shows how the $^2$LMCT undergoes a (slow) intersystem crossing with the IS state and thereafter the system either falls back on the LS state or undergoes a second intersystem crossing and gets trapped in the HS state, as expected for LIESST. Both process are fast and compete.

## 4 Conclusions

The strategy proposed by Papai *et al.* [34] to study to electronic structure and the thermodynamic properties of Fe(II) spin-crossover complexes has been validated for two prototypical Fe(III) complexes, $[Fe(qsal)_2]^+$ and $[Fe(pap)_2]^+$. The use of the B3LYP* functional within the framework of (time-dependent) density functional theory has been proven to be suitable to obtain accurate geometries, vibrational frequencies and relative energies of the states involved in the thermal and light-induced spin-crossover of the two Fe(III) complexes. The adiabatic HS-LS energy difference is in reasonable agreement with the estimate calculated with multiconfigurational wave function techniques (CASSSCF/CASPT2) and the $T_{1/2}$ that we derived by combining the $\Delta E_{HL}$ with the zero-point energy corrections and the entropy contributions is on the same order of magnitude as the experimental transition temperature for spin crossover. The TD-DFT/B3LYP*

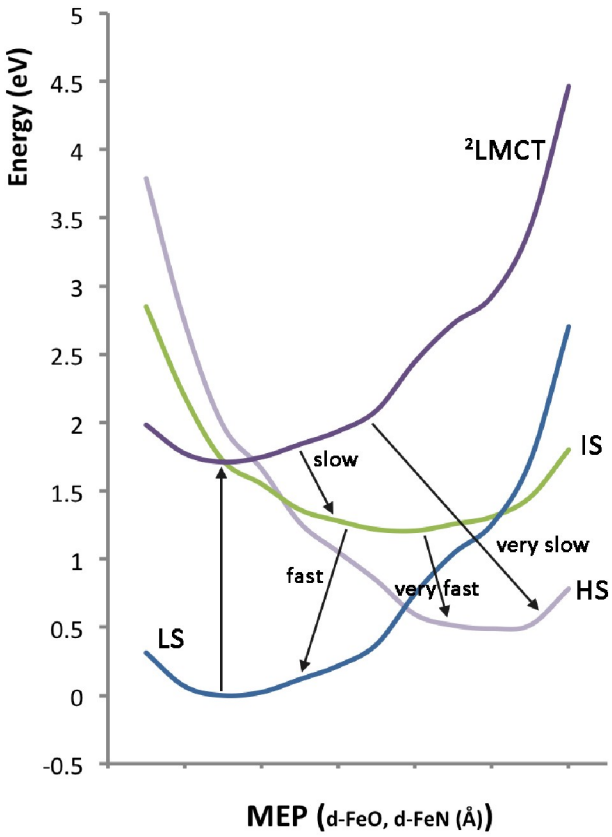


Figure 10: Graphical representation of the photocycle of the $[Fe(qsal)_2]^+$ showing the different deactivation paths.

calculations gives a good account of the absorption spectrum with an intense band of ligand-to-metal charge transfer character in the expected region.

After this pertinent validation, the study of the LIESST mechanism in Fe(III) has been performed. The two-dimensional scan of the energy surface of LS and HS states as function of the Fe-N and Fe-O distances defines an approximate reaction coordinate for the deactivation of the excited doublet state to the final, metastable HS state. Alternative choices such as the Fe-N distances and the changes in the O-Fe-N angle lead to slightly different reaction paths, but the main features are expected to be the same. The TD-DFT calculations along the reaction path define the potential energy curves of the electronic states involved in the LIESST process. We observe that after the excitation of the system in the $^2$LMCT state, it can undergo an intersystem crossing with the IS in the Franck-Condon region and subsequently convert to the HS state via a second intersystem crossing close to the first one. The IS$\rightarrow$LS crossing is found slightly displaced towards the HS minimum along the reaction path.

More information about the deactivation has been obtained by calculating the intersystem crossing rates with the time dependent formulation of Fermi's golden rule as done before in $[Fe(bpy)_3]^{2+}$. In addition to the energy differences and the vibrational modes, one also needs the spin-orbit coupling matrix elements between the electronic states. These were calculated with the state interaction method based on CASSCF wave functions, second-order couplings were incorporated by an effective Hamiltonian treatment. The calculated rates let us propose two competing pathways in the photocycle of the LIESST process. After a relatively slow $^2$LMCT$\rightarrow$IS intersystem crossing, the system can deactivate very rapidly to the final HS state or fall back on the initial LS state. This scenario of two competing pathways is in agreement with the low efficiency of the LS-HS conversion found in experiment. There are several differences with the LIESST mechanism of the Fe(II) complexes. In the first place, the process is expected to be significantly slower because of the small spin-orbit coupling between the $^2$MLCT and the IS state. Secondly, the first intersystem crossing cannot take place in the LMCT manifold as the $^4$LMCT state lies too high in energy, and therefore, necessarily involves a ligand-field quartet state. Finally, the efficiency of the process is much smaller than in the Fe(II) complexes due

to the competition between the IS→LS and IS→HS pathways.

One should be aware that the calculation of the intersystem crossing rates with Ferm's golden rule gives a first rough estimate and that non-adiabatic effects are not included. To obtain a more complete description one should rely on the previously mentioned MCTDH or excited state molecular dynamics methods. However, these methods also have some drawbacks. The quality of the MCTDH results rely critically on the choice of the vibrational modes included int he model Hamiltonian, in contrast to the application of Fermi's rule, which considers all vibrational degrees of freedom. The molecular dynamics with surface hopping are very costly and it is far from trivial to include enough electronic states to scan all possible deactivation paths. A combination of the three schemes would most probably give a more complete description of the photocycle.

## Acknowledgments

Financial support has been provided by the Spanish Administration (Project CTQ2014-51938-P), the Generalitat de Catalunya (Projects 2014SGR199 and Xarxa d'R+D+I en Química Teòrica i Computacional, XRQTC) and the European Union (COST Action ECOSTBio CM1305).

# References

[1] *Spin crossover in Transition Metal Compounds*, ed. P. Gütlich and H. A. Goodwin, Springer-Verlag, 2004, vol. 233-235.

[2] *Spin-Crossover Materials – Properties and Applications*, ed. M. A. Halcrow, Wiley, Chichester, United Kingdom, 2013.

[3] *Spin States in Biochemistry and Inorganic Chemistry: Influence on Structure and Reactivity*, ed. M. Swart and M. Costas, Wiley, Chichester, United Kingdom, 2016.

[4] L. Cambi and L. Szegö, *Ber. Deutsch. Chem. Ges.*, 1931, **64**, 2591.

[5] P. J. van Koningsbruggen, Y. Maeda and H. Oshio, in *Spin crossover*

*in Transition Metal Compounds I*, ed. P. Gütlich and H. A. Goodwin, Springer-Verlag, 2004, vol. 233, pp. 233–259.

[6] M. Nihei, T. Shiga, Y. Maeda and H. Oshio, *Coord. Chem. Rev.*, 2007, **251**, 2606–2621.

[7] J. J. McGarvey and I. Lawthers, *J. Chem. Soc., Chem. Commun.*, 1982, 906–907.

[8] S. Decurtins, P. Gütlich, C. P. Köhler, H. Spiering and A. Hauser, *Chem. Phys. Lett.*, 1984, **105**, 1–4.

[9] A. Hauser, *J. Chem. Phys.*, 1991, **94**, 2741–2748.

[10] A. Hauser, C. Enachescu, L. M. Lawson Daku, A. Vargas and N. Amstutz, *Coord. Chem. Rev.*, 2006, **250**, 1642–1652.

[11] J.-F. Létard, *J. Mater. Chem.*, 2006, **16**, 2550–2559.

[12] M. A. Halcrow, *Chem. Soc. Rev.*, 2008, **37**, 278–289.

[13] C. Boilleau, N. Suaud and N. Guihéry, *J. Chem. Phys.*, 2012, **137**, 224304.

[14] S. Hayami, Z.-z. Gu, M. Shiro, Y. Einaga, A. Fujishima and O. Sato, *J. Am. Chem. Soc.*, 2000, **122**, 7126–7127.

[15] G. Juhász, S. Hayami, O. Sato and Y. Maeda, *Chem. Phys. Lett.*, 2002, **364**, 164–170.

[16] S. Hayami, K. Hiki, T. Kawahara, Y. Maeda, D. Urakami, K. Inoue, M. Ohama, S. Kawata and O. Sato, *Chem. Eur. J.*, 2009, **15**, 3497–3508.

[17] T. Shimizu, Y. Komatsu, H. Kamihata, Y. Lee, A. Fuyuhiro, S. Iijima and S. Hayami, *Journal of Inclusion Phenomena and Macrocyclic Chemistry*, 2011, **71**, 363–369.

[18] M. Clemente-León, E. Coronado, M. López-Jordà, J. C. Waerenborgh, C. Desplanches, H. Wang, J.-F. Létard, A. Hauser and A. Tissot, *J. Am. Chem. Soc.*, 2013, **135**, 8655–8667.

[19] K. D. Murnaghan, C. Carbonera, L. Toupet, M. Griffin, M. M. Dîrtu, C. Desplanches, Y. Garcia, E. Collet, J.-F. Létard and G. G. Morgan, *Chem. Eur. J.*, 2014, **20**, 5613–5618.

[20] W. Gawelda, A. Cannizzo, V.-T. Pham, F. van Mourik, C. Bressler and M. Chergui, *J. Am. Chem. Soc.*, 2007, **129**, 8199–8206.

[21] C. Consani, M. Premont-Schwarz, A. ElNahhas, C. Bressler, F. van Mourik, A. Cannizzo and M. Chergui, *Angew. Chem. Int. Ed.*, 2009, **48**, 7184–7187.

[22] A. Cannizzo, C. J. Milne, C. Consani, W. Gawelda, C. Bressler, F. van Mourik and M. Chergui, *Coord. Chem. Rev.*, 2010, **254**, 2677–2686.

[23] N. Huse, H. Cho, K. Hong, L. Jamula, F. M. F. de Groot, T. K. Kim, J. K. McCusker and R. W. Schoenlein, *J. Phys. Chem. Lett.*, 2011, **2**, 880–884.

[24] W. Zhang, R. Alonso-Mori, U. Bergmann, C. Bressler, M. Chollet, A. Galler, W. Gawelda, R. G. Hadt, R. W. Hartsock, T. Kroll, K. S. Kjær, K. Kubiček, H. T. Lemke, H. W. Liang, D. A. Meyer, M. M. Nielsen, C. Purser, J. S. Robinson, E. I. Solomon, Z. Sun, D. Sokarasa, T. B. van Driel, G. Vankó, T.-C. Weng, D. Zhu and K. J. Gaffney, *Nature*, 2014, **509**, 345–348.

[25] G. Auböck and M. Chergui, *Nature Chem.*, 2015, **7**, 629–633.

[26] J. K. McCusker, K. N. Walda, R. C. Dunn, J. D. Simon, D. Magde and D. N. Hendrickson, *J. Am. Chem. Soc.*, 1993, **115**, 298–307.

[27] C. Sousa, C. de Graaf, A. Rudavskyi, R. Broer, J. Tatchen, M. Etinski and C. M. Marian, *Chem. Eur. J.*, 2013, **19**, 17541–17551.

[28] E. W. T. Yemeli, G. R. Blake, A. P. Douvalis, T. Bakas, G. O. R. Alberda van Ekenstein and P. J. van Koningsbruggen, *Chem. Eur. J.*, 2010, doi: 10.1002/chem.201002100.

[29] H. Ando, Y. Nakao, H. Sato and S. Sakaki, *J. Phys. Chem. A*, 2007, **111**, 5515–5522.

[30] M. Etinski, J. Tatchen and C. M. Marian, *J. Chem. Phys.*, 2011, **134**, 154105.

[31] M. Reiher, O. Salomon and B. A. Hess, *Theor. Chem. Acc.*, 2001, **107**, 48–55.

[32] M. Swart, *J. Chem. Theory Comput.*, 2008, **4**, 2057–2066.

[33] K. P. Kepp, *Coord. Chem. Rev.*, 2013, **257**, 196–209.

[34] M. Pápai, G. Vankó, C. de Graaf and T. Rozgonyi, *J. Chem. Theory Comput.*, 2013, **9**, 509–519.

[35] C. de Graaf and C. Sousa, *Chem. Eur. J.*, 2010, **16**, 4550–4556.

[36] F. Neese, *WIREs Comput. Mol. Sci.*, 2012, **2**, 73–78.

[37] F. Weigend and R. Ahlrichs, *Phys. Chem. Chem. Phys.*, 2005, **7**, 3297.

[38] R. Izsak and F. Neese, *J. Chem. Phys.*, 2011, **135**, 144105.

[39] T. Petrenko, S. Kossmann and F. Neese, *J. Chem. Phys.*, 2011, **134**, 054116.

[40] C. Adamo and V. Barone, *J. Chem. Phys.*, 1999, **110**, 6158–6170.

[41] R. Ahlrichs, M. Bär, M. Häser, H. Horn and C. Kölmel, *Chem. Phys. Lett.*, 1989, **162**, 165.

[42] O. Treutler and R. Ahlrichs, *J. Chem. Phys.*, 1995, **102**, 346.

[43] F. Furche, R. Ahlrichs, C. Hättig, W. Klopper, M. Sierka and F. Weigend, *WIREs Comput. Mol. Sci.*, 2014, **1**, 91–100.

[44] *TURBOMOLE V6.6 2014, a development of University of Karlsruhe and Forschungszentrum Karlsruhe GmbH, 1989-2007, TURBOMOLE GmbH, since 2007; available from* `http://www.turbomole.com`.

[45] F. Aquilante, L. De Vico, N. Ferré, G. Ghigo, P.-Å. Malmqvist, P. Neograd y, T. B. Pedersen, M. Pitoňák, M. Reiher, B. O. Roos, L. Serrano-Andrés, M. Urban, V. Veryazov and R. Lindh, *J. Comput. Chem.*, 2010, **31**, 224–247.

[46] B. O. Roos, R. Lindh, P.-Å. Malmqvist, V. Veryazov and P.-O. Widmark, *J. Phys. Chem. A*, 2004, **108**, 2851–2858.

[47] B. O. Roos, R. Lindh, P.-Å. Malmqvist, V. Veryazov and P.-O. Widmark, *J. Phys. Chem. A*, 2005, **109**, 6575–6579.

[48] F. Aquilante, T. B. Pedersen and R. Lindh, *J. Chem. Phys.*, 2007, **126**, 194106.

[49] F. Aquilante, P.-Å. Malmqvist, T. B. Pedersen, A. Ghosh and B. O. Roos, *J. Chem. Theory Comput.*, 2008, **4**, 694–702.

[50] B. A. Hess, *Phys. Rev. A*, 1986, **33**, 3742–3748.

[51] P.-Å. Malmqvist and B. O. Roos, *Chem. Phys. Lett.*, 1989, **155**, 189–194.

[52] P.-Å. Malmqvist, B. O. Roos and B. Schimmelpfennig, *Chem. Phys. Lett.*, 2002, **357**, 230–240.

[53] B. O. Roos and P.-Å. Malmqvist, *Phys. Chem. Chem. Phys.*, 2004, **6**, 2919–2927.

[54] K. Andersson, P.-Å. Malmqvist and B. O. Roos, *J. Chem. Phys.*, 1992, **96**, 1218–1226.

[55] K. Pierloot and S. Vancoillie, *J. Chem. Phys.*, 2006, **125**, 124303.

[56] N. Forsberg and P.-Å. Malmqvist, *Chem. Phys. Lett.*, 1997, **274**, 196–204.

[57] M. Kepenekian, V. Robert, B. Le Guennic and C. de Graaf, *J. Comput. Chem.*, 2009, **30**, 2327–2333.

[58] A. Bousseksou, J. J. McGarvey, F. Varret, J.-A. Real, J.-P. Tuchagues, A. C. Dennis and M.-L. Boillot, *Chem. Phys. Lett.*, 2000, **318**, 409–416.

[59] S. Hayami, Z.-z. Gu, H. Yoshiki, A. Fujishima and O. Sato, *J. Am. Chem. Soc.*, 2001, **123**, 11644–11650.

[60] P. Gütlich, H. Köppen, R. Link and H. G. Steinhäuser, *J. Chem. Phys.*, 1979, **70**, 3977–3983.

[61] M. Reiher, *Inorg. Chem.*, 2002, **41**, 6928–6935.

[62] R. Boča and W. Linert, *Monatsh Chem.*, 2003, **134**, 199–216.

[63] J. Cirera and F. Paesani, *Inorg. Chem.*, 2012, **51**, 8194–8201.

[64] A. Rudavskyi, C. Sousa, C. de Graaf, R. W. A. Havenith and R. Broer, *J. Chem. Phys.*, 2014, **140**, 184318.

[65] S. Alvarez, D. Avnir, M. Llunell and M. Pinsky, *New J. Chem.*, 2002, **26**, 996–1009.

[66] S. Alvarez, *J. Am. Chem. Soc.*, 2003, **125**, 6795–6802.

[67] M. Cammarata, R. Bertoni, M. Lorenc, H. Cailleau, S. Di Matteo, C. Mauriac, S. F. Matar, H. Lemke, M. Chollet, S. Ravy, C. Laulhé, J.-F. Létard and E. Collet, *Phys. Rev. Lett.*, 2014, **113**, 227402.

[68] R. Bertoni, M. Cammarata, M. Lorenc, S. F. Matar, J.-F. Létard, H. T. Lemke and E. Collet, *Acc. Chem. Res.*, 2015, **48**, 774–781.

[69] S. Saureu and C. de Graaf, *Chem. Phys.*, 2014, **428**, 59–66.

[70] B. Ordejón, C. de Graaf and C. Sousa, *J. Am. Chem. Soc.*, 2008, **130**, 13961–13968.

[71] N. Suaud, M.-L. Bonnet, C. Boilleau, P. Labèguerie and N. Guihéry, *J. Am. Chem. Soc.*, 2009, **131**, 715–722.

[72] L. M. Lawson Daku, F. Aquilante, T. W. Robinson and A. Hauser, *J. Chem. Theory Comput.*, 2012, **8**, 4216–4231.

[73] K. Andersson, P.-Å. Malmqvist, B. O. Roos, A. J. Sadlej and K. Wolinski, *J. Phys. Chem.*, 1990, **94**, 5483–5488.

[74] M. F. Tweedle and L. J. Wilson, *J. Am. Chem. Soc.*, 1976, **98**, 4824–4834.

[75] S. Schenker, A. Hauser and R. M. Dyson, *Inorg. Chem.*, 1996, **35**, 4676–4682.

[76] A. Domingo, C. Sousa and C. de Graaf, *Dalton Trans.*, 2014, **43**, 17838–17846.

[77] S. Iuchi and N. Koga, *J. Chem. Phys.*, 2014, **140**, 024309.

[78] B. A. Hess, C. M. Marian, U. Wahlgren and O. Gropen, *Chem. Phys. Lett.*, 1996, **251**, 365–371.

[79] J.-P. Malrieu, R. Caballol, C. J. Calzado, C. de Graaf and N. Guihéry, *Chem. Rev.*, 2014, **114**, 429–492.

[80] S. Mai, P. Marquetand and L. González, *Int. J. Quantum Chem.*, 2015, **115**, 1215–1231.

[81] C. Daniel, *Coord. Chem. Rev.*, 2015, **282-283**, 19–32.

[82] C. Gourlaouen, J. Eng, M. Otsuka, E. Gindensperger and C. Daniel, *J. Chem. Theory Comput.*, 2015, **11**, 99–110.

[83] G. Capano, T. J. Penfold, U. Röthlisberger and I. Tavernelli, *Chimia*, 2014, **68**, 227–230.

[84] G. Capano, U. Rothlisberger, I. Tavernelli and T. J. Penfold, *J. Phys. Chem. A*, 2015, **119**, 7026–7037.

[85] L. Yu, C. Xu, Y. Lei, C. Zhu and Z. Wen, *Phys. Chem. Chem. Phys.*, 2014, **16**, 25883–25895.

[86] W. Ouyang, W. Dou and J. E. Subotnik, *J. Chem. Phys.*, 2015, **142**, 084109.